A Kinetic Model of Membrane Formation by CVD of SiO_2 and Al_2O_3

Michael Tsapatsis and George R. Gavalas
Div. of Chemistry and Chemical Engineering, California Institute of Technology, Pasadena, CA 91125

Silica and alumina layers deposited onto the walls of porous Vycor tubes by chloride hydrolysis in an opposing reactants geometry have been characterized by scanning electron microscopy and electron microprobe analysis. The layers are asymmetric, having a long tail toward the side of the chloride flow and a sharp boundary at the other side. The deposit thickness is several tenths of microns, while the totally plugged region is of order of 1 micron.

A model has been developed describing reaction, diffusion and evolution of the porous structure in the Vycor substrate due to the accumulation of the solid product. The deposition reaction is described by transient kinetics in terms of the concentrations of silanol and chloride groups in the product layer, as well as the concentrations of the gaseous reactants. The model is capable of generating deposit profiles in good agreement with those measured by electron microprobe analysis.

Introduction

Chemical vapor deposition (CVD) is a versatile technique widely used in the manufacture of electronic and optical devices. It has also been used for making the electrolyte layers of solid oxide fuel cells (Isenberg, 1981; Carolan and Michaels, 1987). CVD of SiO_2 and other oxides on porous Vycor tubes has been used in our laboratory to prepare hydrogen membranes capable of operation at elevated temperatures. In our first experiments we used SiH_4 oxidation to deposit SiO_2 (Gavalas et al., 1989), but later turned to the hydrolysis of $SiCl_4$, $TiCl_4$, or $AlCl_3$, BCl_3 to deposit SiO_2, TiO_2, Al_2O_3, and B_2O_3, all selectively permeable to hydrogen (Tsapatsis et al., 1991). Deposition was carried out in the opposing reactants geometry, that is, by applying flows of the chloride and water at opposite sides of the porous tube wall. Deposition of SiO_2, but not of the other oxides, was also possible in the one-sided geometry: both reactants flowing at the same side of the porous support.

The one-sided geometry is used in film deposition on nonporous substrates and in chemical vapor infiltration (CVI) in porous substrates. When the latter process is employed for composite materials fabrication, it is essential that the product solid fills the porous substrate completely. By contrast, membrane preparation requires the deposit layer to be as thin as possible to achieve high flux of the permeate gas. Scanning electron microscopy and electron microprobe analysis of the SiO_2 and Al_2O_3 deposit layers deposited within the porous substrate show that the density of the product oxide (SiO_2, Al_2O_3) is not uniform across the deposit layer. There is a sharp peak at the point of pore plugging and a much wider region of lower deposit density. Only the region of pore plugging serves a useful membrane function, while the partially plugged region decreases the membrane permeance without improving materially the membrane selectivity. The present study was focused on understanding how the density profile of the deposit layer is influenced by the deposition chemistry and the operating conditions, with the goal of preparing improved membranes.

Deposition within a porous substrate involves reaction, diffusion, and gradual pore closure, a problem that has received considerable attention in the chemical engineering literature during the last ten years in the context of lime sulfation and other gas-solid reactions. In this article, we emphasize the deposition kinetics and treat the transport features of the problem in a simple fashion. Depending on the gas composition and pressure, the nature of the substrate, the temperature, and the contact scheme, CVD processes may be dominated by homogeneous or heterogeneous reactions, or both may be equally important. In the opposing reactants deposition employed in our experiments, heterogeneous reactions are expected to be dominant because of the high surface area of the microporous substrate (mean pore size, 40 Å; BET surface area, 200 m^2/g). In one-sided deposition, on the other hand, gas-phase reactions outside of the substrate may become im-

portant and may, in fact, prevent the deposition of a permselective layer. Such phenomena seem to be the case with the $AlCl_3$—H_2O and $TiCl_4$—H_2O systems (Tsapatsis et al., 1991).

Heterogeneous kinetics are often formulated assuming that the surface is at pseudosteady state with respect to the fluid phase, thus permitting the expression of the reaction rate solely in terms of gaseous concentrations. Such pseudosteady kinetics are employed commonly to describe CVD and CVI (Carolan and Michaels, 1987; Sotirchos, 1991). The pseudosteady assumption is valid provided that the characteristic time of deposition is much larger than the characteristic relaxation time of surface species concentrations. Otherwise, the surface reaction must be described by transient kinetics. In the deposition of SiO_2, for example, a surface exposed to gaseous $SiCl_4$ and H_2O might eventually develop a steadily growing deposit layer with constant surface concentration of reactive groups. After this steady surface structure has been attained, the deposition rate will become a function solely of the gaseous reactant concentrations. In the problem at hand, however, the deposit layer can only grow to a few layers before pore closure; therefore, the role of the first few layers in determining the final deposit characteristics might be important in the sense that significant pore restriction is caused even by a single layer. On the contrary, this would not be the case in a macroporous substrate when hundreds or thousands of layers are deposited before pore closure. Since the first few layers are developed under unsteady conditions, the emphasis of the present work is on the transient kinetics of deposition.

Experimental Apparatus and Procedure

The apparatus for opposing reactants chemical vapor deposition is described in detail elsewhere (Gavalas et al., 1989). A schematic diagram is shown in Figure 1. The reactor consists of a porous Vycor tube inside a nonporous quartz tube (12 mm ID). The Vycor tube (7 mm OD, 1.1—mm wall thickness, 0.30 void fraction, and 40 Å mean pore diameter) supplied by Corning Inc. is welded from either side with nonporous quartz tube sections to permit connection with metal fittings to the feed gas lines. The chlorides were supplied by Aldrich Chemical Co. with 99.999% purity for $SiCl_4$ and 99.99% purity for $AlCl_3$. A chloride reactant stream $SiCl_4$—N_2 or $AlCl_3$—N_2 of the desired composition was generated by passing a stream of nitrogen through a bubbler or sublimator containing $SiCl_4$ or $AlCl_3$ and held at the appropriate temperature. The water reactant stream was likewise generated by passing N_2 through a water bubbler. Typical flow rates of N_2 were 50–100 cm^3/min for each stream. Typical reactant mol fractions were 0.1-0.35 and were calculated assuming equilibrium at the bubblers.

Before deposition the tubes were heated gradually to 600°C and maintained at that temperature overnight under oxygen flow to remove organic impurities and establish a common concentration of surface hydroxyl groups for all experiments.

Scanning electron microscopy

Scanning electron microscopy (SEM) analysis of tubes carrying the deposited layers was carried out by a CamScan scanning electron microscope operating at 20 kV. The samples (sections of the tubes after deposition) were prepared by first casting in epoxy, and then polishing and coating by carbon or gold to eliminate sample charging. Some tube cross-sections were also examined by electron microprobe analysis (EMA), using a Jeol 733 Superprobe electron microscope with wavelength dispersive spectroscopy detection (WDS). When a focused electron beam was used we observed sample burning which did not significantly affect the analysis of Al_2O_3 or TiO_2 deposits, but was a major problem when analyzing SiO_2 deposit on Vycor. Thus for most of the SiO_2 deposit analysis, a 10-μm beam was used to avoid sample burning. This resulted in a lower resolution for the tracing of SiO_2 layers.

Experimental Results

Permeation coefficients (permeances) of hydrogen and ni-

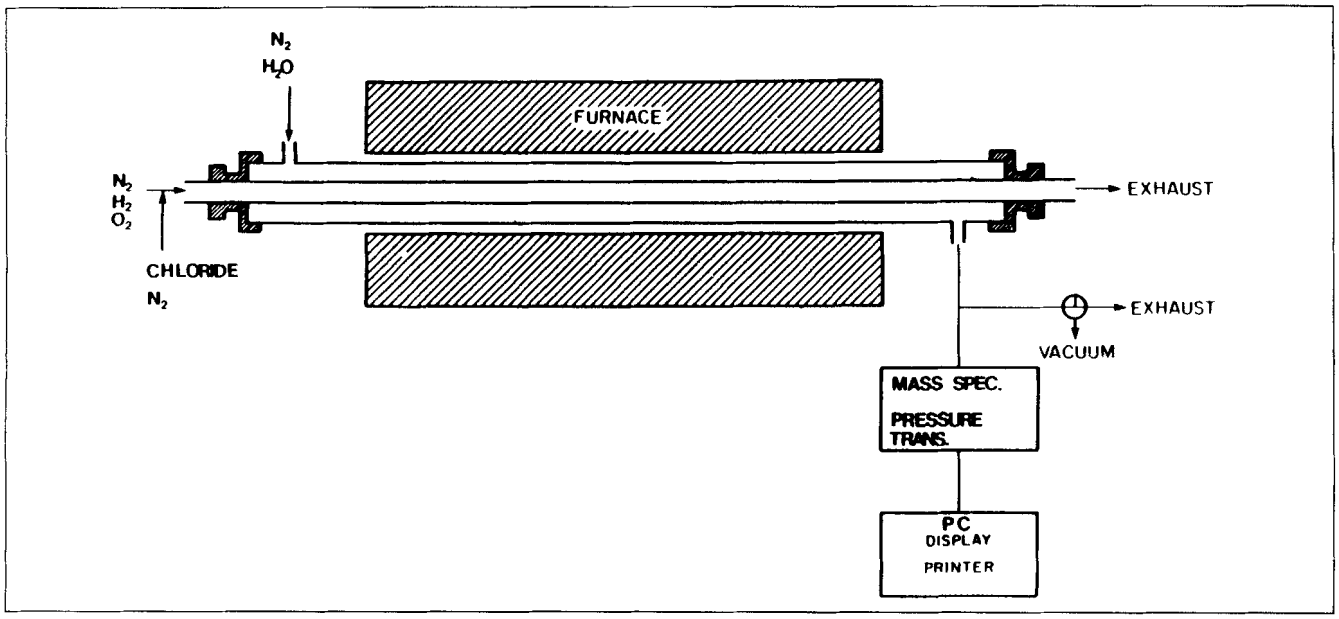

Figure 1. Deposition system.

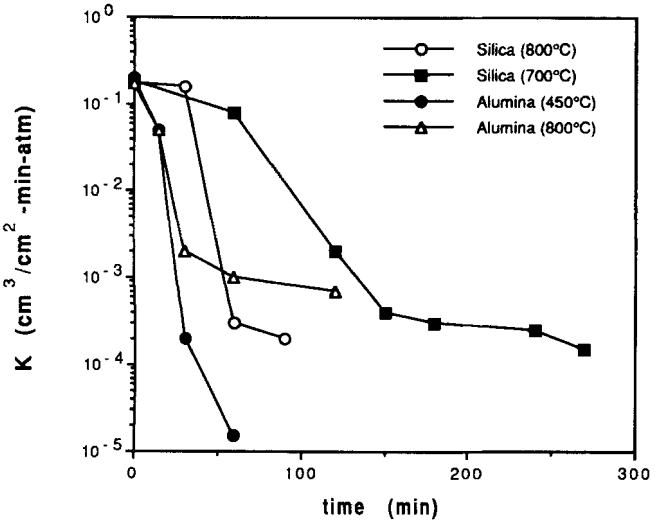

Figure 2. Evolution of N_2 permeation rate coefficients (measured at deposition temperature).

Alumina deposition at 450°C (●) and 800°C (Δ), using 8% H_2O—N_2 and 20% $AlCl_3$—N_2 in opposing reactants geometry. Silica deposition at 800°C(O) and 700°C(■), using 7% H_2O—N_2 and 30% $SiCl_4$—N_2 in opposing reactants geometry.

trogen through SiO_2 and Al_2O_3 membranes are given elsewhere (Tsapatsis et al., 1991). Here we consider only the N_2 permeation coefficient as a measure of pore plugging. Figure 2 shows typical results for the evolution of the N_2 permeation coefficient during Al_2O_3 and SiO_2 deposition. The decline of the N_2 flux, initially slow, accelerates, and then becomes slow once more. The end of the rapid decline period is evidently caused by the elimination of all Knudsen diffusion paths connecting the two sides of the tube wall, that is, by the loss of connectivity. Once the open Knudsen paths have been eliminated, the reaction rate drops to a very low residual value controlled by activated flux of water through the deposit layer. This residual reaction takes place at the chloride side, since the diffusion coefficient of the larger chloride molecule through the deposit layer is much smaller than that of water. We shall refer to the elimination of continuous Knudsen paths as "pore plugging" and shall define it operationally by the time when the nitrogen flux has declined to one hundredth of its initial value. Typical times for pore plugging are 15 min for Al_2O_3 deposition at 450°C, 30 min for Al_2O_3 deposition at 800°C, and 1 h for SiO_2 deposition at 800°C.

Figure 3a shows an SEM photograph of an Al_2O_3 membrane. The darker region located near the inner radius reveals the presence of aluminum. The white line at the end of that region is believed to be a step created on the sample surface during polishing due to the harder alumina-rich region. A typical Al_2O_3/SiO_2 profile obtained by EMA is shown in Figure 3b. The oxide ratio is derived based on the assumption that all Al is present as Al_2O_3. The deposit layer has strongly asymmetric shape and is located near the side of chloride flow, in agreement with previously reported EMA measurements (Tsapatsis et al., 1991). The deposit layer is spread over several tens of microns, but the completely plugged region is much thinner, probably of order 1 micron, as evidenced by the sharp maximum of the Al_2O_3/SiO_2 ratio located on the white line of the SEM photographs.

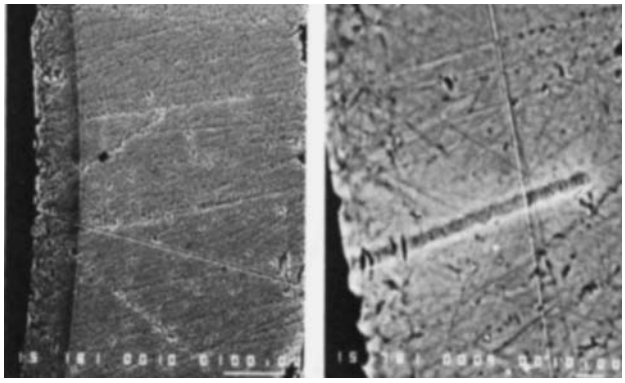

Figure 3a. SEM micrograph of an Al_2O_3 membrane at two different magnifications: bars are 100μm (left) and 10μm (right).

Membrane prepared at 800°C by opposing reactants deposition with 20% $AlCl_3$—N_2 and 7% H_2O—N_2.

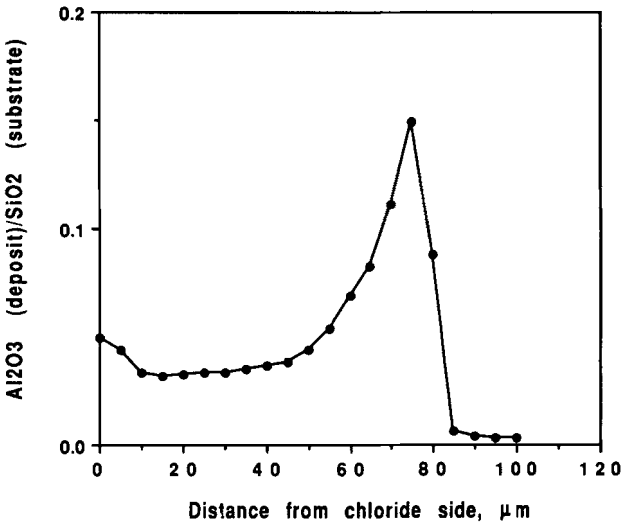

Figure 3b. Mass ratio of Al_2O_3 (deposit) to SiO_2 (substrate) obtained by electron microprobe analysis of the membrane shown in Figure 3a.

Figure 4a shows the radial profile of the Al_2O_3/SiO_2 ratio after 3, 10 and 15 min of deposition. The profile, initially monotonically decreasing, at a later time develops a maximum, which sharpens with the progress of deposition. Figures 4b-4d show the SEM photographs. The end of the deposit layer can be traced by the position of the white line. Figure 5 shows the ratio of deposited SiO_2 to substrate SiO_2 across a tube after pore plugging. The weight of deposited SiO_2 is derived based on the assumption that all Si deposited is SiO_2. We had previously found that SiO_2 density of untreated Vycor tubes varies over the cross-section of the tube. The ratio plotted in Figure 5 is based on the measured SiO_2 density profile of the untreated tube. As in Figure 3b, the deposit density is highly asymmetrical about the location of the maximum. However, the overall thickness of the layer is considerably larger than that of Figure 3b.

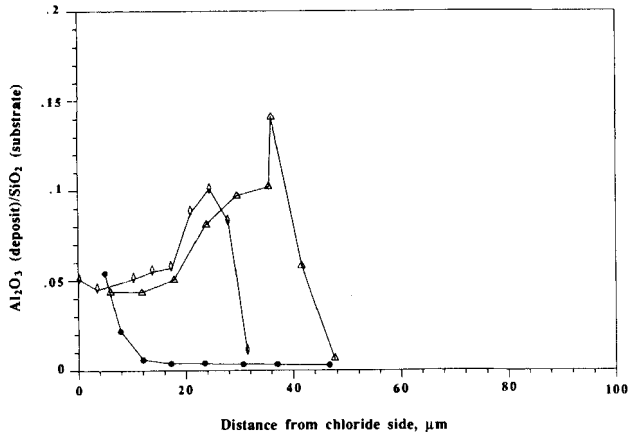

Figure 4a. Electron microprobe analysis of Vycor cross-sections subjected to Al_2O_3 deposition in the opposing reactants geometry.

At 450°C with 20% $AlCl_3$—N_2 and 7% H_2O—N_2 for 3 min (O), 10 min (◇) and 15 min (Δ).

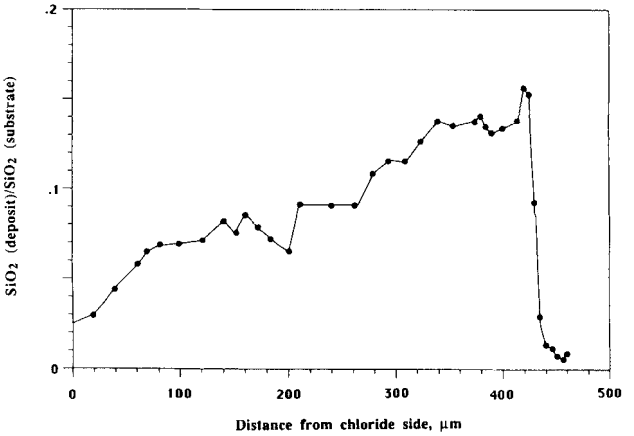

Figure 5. Electron microprobe line scan of a tube cross-section after SiO_2 deposition in opposing reactants geometry using 30% $SiCl_4$—N_2 and 7% H_2O—N_2, for 1 h.

The highest value of the Al_2O_3 (deposit)/SiO_2 (substrate) and SiO_2 (deposit)/SiO_2 (substrate) mass ratios measured on the EMA traces for samples that underwent pore plugging is about 0.17. Complete pore filling (to void fraction zero), on the other hand, corresponds to a ratio of 0.43 for SiO_2 and 0.58 for Al_2O_3 based on true (helium) densities of 2.1 for SiO_2 (corresponding to reported densities of SiO_2 films deposited by SiH_4 oxidation) and 2.85 for Al_2O_3 (corresponding to reported densities for γ—Al_2O_3). There are several possible reasons for this discrepancy. The first possibility is that the layers deposited in the opposing reactants geometry have lower densities than the nominal densities used in the calculations. Second, sample polishing would smear and blunt the deposit at the peak, especially if the peak is sharp. Third, the electron beam excites a finite volume in the sample introducing a form of spatial averaging, which would reduce the measured intensity at the narrow plugged region. Moreover, the experimental uncertainty for the SiO_2 analysis is greater than for Al_2O_3, because the calculations for the former require the analysis of two different Vycor samples, while for the latter the EMA scan of a single sample provides directly the deposit to substrate ratio. Although these uncertainties are significant, it is unlikely that they are sufficient to fully account for the difference between the measured deposit density and the density corresponding to complete pore filling. A major part of this difference must be attributed to interruption of connectivity at a nonzero void fraction, as expected from percolation theory.

To explore the role of the initial chemical structure of the substrate surface on the course of deposition we performed

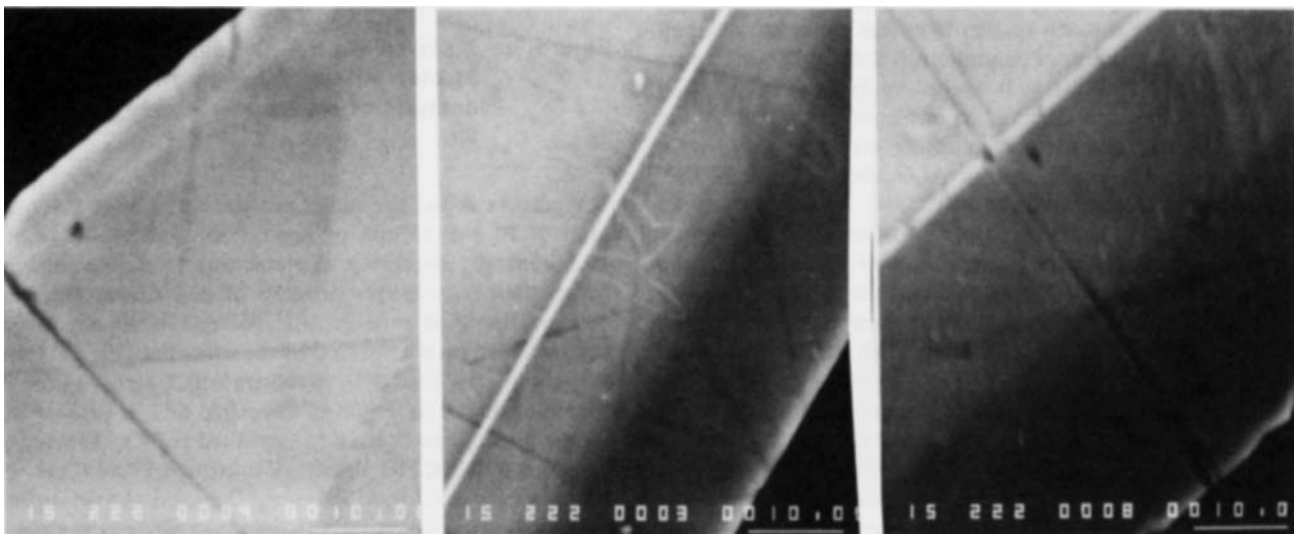

Figure 4b. SEM image corresponding to Figure 4a for 3 min.

Figure 4c. SEM image corresponding to Figure 4a for 10 min.

Figure 4d. SEM image corresponding to Figure 4a for 15 min.

the following additional experiment. The porous Vycor support was first exposed to a dry stream of $AlCl_3$—N_2, which reacts to replace surface OH groups with Cl groups as follows:

$$AlCl_3(g) + Si—OH(s) = Si—O—Al—(Cl)_2(s) + HCl(g) \quad (1)$$

The dehydroxylated or partially dehydroxylated support was then subjected to the usual opposing reactant deposition of Al_2O_3. The EMA analysis of the resulting deposit layer produced the results shown in Figure 6. The peak has shifted toward the water side and the steep decline faces the chloride side, in contrast with the peak shapes observed in Figures 3 to 5. The drastic change of the deposit profile reveals the importance of the substrate surface chemistry.

Model Formulation

Reaction mechanism for SiO_2 formation

The role of homogeneous and heterogeneous reactions in one-sided and opposing reactants deposition has been discussed in a previous report (Tsapatsis et al., 1991). Previous kinetic experiments suggest that the homogeneous reaction between $SiCl_4$ and water is slow and that SiO_2 deposition on high surface area silica takes place by a heterogeneous mechanism that can be described by the following simplified scheme (Hair and Hertl, 1969, 1973; Armistead and Hockey, 1967):

$$Si—OH(s) + SiCl_4(g) = 3Si—Cl(s) + HCl(g) \quad (2)$$

$$Si—Cl(s) + H_2O(g) = Si—OH(s) + HCl(g) \quad (3)$$

$$Si—OH(s) + Si—OH(s) = Si—O—Si(s) + H_2O(g) \quad (4)$$

$$Si—OH(s) + Si—Cl(s) = Si—O—Si(s) + HCl(g) \quad (5)$$

where Si—OH(s) represents a surface hydroxyl group (silanol), Si—Cl(s) a surface chloride group, and Si—O—Si(s) a siloxane bridge on the solid. In this notation we count surface —OH and —Cl groups and not silicon atoms. Equation 2 could be written more analytically as:

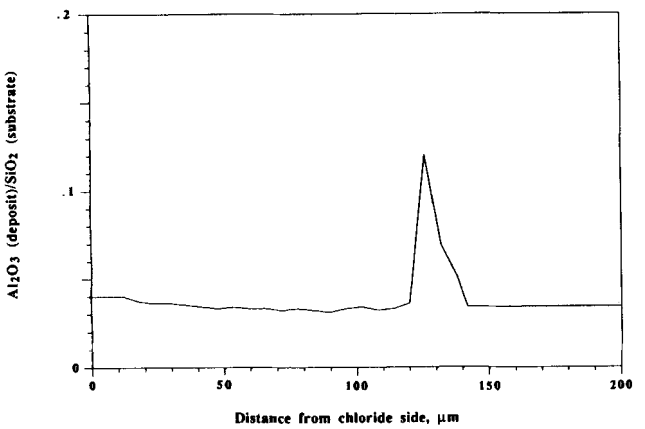

Figure 6. Electron microprobe line scan of a tube cross-section subjected to Al_2O_3 deposition after pretreatment by $AlCl_3$.

$$Si—OH(s) + SiCl_4(g) = Si—O—Si\begin{matrix}Cl\\ <\\ Cl\end{matrix}(s) + HCl(g) \quad (2a)$$

In limiting the reaction network to the above four steps, we have neglected the attack by $SiCl_4$ on siloxane bonds leading to the direct chlorination:

$$SiCl_4 + Si—O—Si(s) = Si—Cl(s) + Si—O—SiCl_3(s) \quad (6)$$

which has been previously reported, but not quantified (Morrow and Code, 1976; Bunker et al., 1989). We have also not distinguished among different types of surface —OH groups (isolated, geminal, and hydrogen-bonded) which are known to have different reactivities toward $SiCl_4$ and other chlorides. According to Eq. 2, the chloride initially reacts with the Vycor surface even in the absence of water (until all OH groups are consumed). That reaction affects the chloride concentration profile and consequently the overall deposition process.

Reaction mechanism for Al_2O_3 formation

The reports of Peri (1966) and Peri and Hensley (1968) on reactions of $AlCl_3$ with surface —OH groups suggest that a reaction analogous to Eq. 2 takes place between gaseous $AlCl_3$ and silica. However, IR examination of a silica sample treated by $AlCl_3$ and subsequently exposed to H_2O disclosed Si—OH, rather than Al—OH groups (Peri, 1966; Peglar et al., 1971). The absence of Al—OH may be due to rapid condensation or the transfer of these groups to silicon atoms. In view of the uncertainty about the precise reactions of $AlCl_3$ with silica, we have not developed specific rate expressions for the formation of Al_2O_3. Moreover, the homogeneous reaction between $AlCl_3$ and H_2O may play some role despite the large surface area and the low concentration of reactants in the deposition region (Wong and Robinson, 1970). Because of this lack of specific kinetic information, we have not implemented the model for alumina deposition. We note, however, that the density profiles of the Al_2O_3 layer as well as those from TiO_2 deposition reported elsewhere (Tsapatsis et al., 1991) have some common features with those of SiO_2, especially the slow increase followed by the steep decline in the direction from the chloride side to the water side, suggesting similarities in the deposition mechanisms.

Formulation of kinetics and species balances

The silanol and chloride groups initially can be considered as surface species. As the deposit builds up, however, these groups become distributed throughout the volume of the deposit layer. Because of this unusual feature, the concentration of silanol and chloride groups will be given in mols per unit volume.

The species balances will be formulated treating reactions 2 through 5 as elementary and using the rate expressions:

$$r_1 = k_1 C_1 S_{OH} \quad (7)$$

$$r_2 = k_2 C_2 S_{Cl} \quad (8)$$

$$r_3 = k_3' S_{OH}^2 \quad (9)$$

$$r_4 = k_4' S_{OH} S_{Cl} \tag{10}$$

where S_{OH} and S_{Cl} are the concentrations of the —OH and —Cl groups in mols per unit total volume, and the r_1 are expressed in mols per unit total volume per unit time. As suggested in the literature (Hair and Hertl, 1969, 1973; Armistead and Hockey, 1967), the reactions are considered irreversible with HCl being unable to attack the silica deposit (Iller, 1979). It is implicitly assumed that all —OH and —Cl groups within the deposit layer are equally accessible to the gaseous molecules, a reasonable assumption in view of the few monolayer thicknesses of the deposit layer. Unlike reactions 2 and 3, reactions 4 and 5 are assumed to be second-order in the condensed species —OH and —Cl. It should be noted here that we consider condensation reactions taking place in the whole volume of the deposit. This is in accordance with the assumption that all OH and Cl species are accessible to gaseous reactants. In other words, the condensation reactions are considered as solid-state reactions with rates expressed per unit volume of the deposit layer per unit time. If $\phi = \epsilon_0 - \epsilon$ is the volume fraction of the deposit layer with respect to the total volume, then the rate of reaction 4 in mols per unit volume of the deposit layer per unit time is given by:

$$\frac{r_3}{\phi} = k_3 \left(\frac{S_{OH}}{\phi} \right)^2 \tag{11}$$

and similarly for reaction 5, with k_3 and k_4 being intrinsic rate constants. Thus, the rate parameters k_3' and k_4' in Eqs. 9 and 10 are functions of the extent of deposition,

$$k_3' = \frac{k_3}{\epsilon_0 - \epsilon}, \qquad k_4' = \frac{k_4}{\epsilon_0 - \epsilon} \tag{12}$$

Equations 9, 10 and 12 hold only after the deposit layer has attained a small, but finite, thickness ($\epsilon_0 - \epsilon > 0$). Initially there are no chloride groups, and the silanol groups have stabilized to some fixed concentration by virtue of the thermal pretreatment. The section on Numerical Results and Discussion describes the initialization of the integration.

The use of two concentrations S_{OH} and S_{Cl} to characterize the deposit layer is a drastic approximation since it ignores the role of the geometric arrangement (such as proximity) of these immobile species. Such effects cannot be represented by classical kinetics and will not be considered here.

We have chosen to represent diffusion and pore constriction by a classical model, ignoring the statistical or percolative aspects of pore connectivity. The EMA results shown in the previous section indicate that connectivity is, in fact, interrupted at some nonzero void fraction. However, the quantification of connectivity and the percolation threshold does not appear practical without additional experimentation, specifically addressed to these issues, or without additional empiricism and mathematical complication.

The conventional reaction-diffusion problem is now formulated using the rate expressions (Eqs. 7-12) and neglecting the curvature of the tube wall to obtain the following balances for the gas-phase and condensed-phase species.

$$\frac{\partial}{\partial x}\left[D_1(\epsilon) \frac{\partial C_1}{\partial x} \right] = k_1 C_1 S_{OH} \tag{13}$$

$$\frac{\partial}{\partial x}\left[D_2(\epsilon) \frac{\partial C_2}{\partial x} \right] = k_2 C_2 S_{Cl} - \frac{k_3}{\epsilon_0 - \epsilon} S_{OH}^2 \tag{14}$$

$$\frac{\partial S_{OH}}{\partial t} = -k_1 C_1 S_{OH} + k_2 C_2 S_{Cl} - \frac{1}{\epsilon_0 - \epsilon}(2k_3 S_{OH}^2 + k_4 S_{OH} S_{Cl}) \tag{15}$$

$$\frac{\partial S_{Cl}}{\partial t} = 3k_1 C_1 S_{OH} - k_2 C_2 S_{Cl} - \frac{k_4}{\epsilon_0 - \epsilon} S_{OH} S_{Cl} \tag{16}$$

Equations 13 and 14 neglect the gas-phase accumulation term, an approximation justified by comparison of the observed times for pore plugging, which were on the order of 30 min, with the characteristic time for gaseous diffusion, which was estimated to be on the order of a few seconds.

The progress of deposition can be characterized by the instantaneous void fraction ϵ computed from the amount of silicon in the deposit layer using some value for the molar volume per silicon atom. For this purpose, we shall ignore the differences among the molar volumes of silicon atoms associated with different groups and use the volume v corresponding to undensified SiO_2 produced by chemical vapor deposition, so that:

$$\frac{\partial \epsilon}{\partial t} = -v k_1 C_1 S_{OH} \tag{17}$$

The initial and boundary conditions associated with Eqs. 13 through 17 are:

$$t = 0: \; S_{OH} = S_{OH}^{\circ}, \; S_{Cl} = 0, \; \epsilon = \epsilon_o \tag{18}$$

$$x = 0: \; \ell_1 (C_{10} - C_1) = -D_1 \frac{\partial c_1}{\partial x} \tag{19}$$

$$\ell_2 C_2 = D_2 \frac{\partial c_2}{\partial x} \tag{20}$$

$$x = L: \; \ell_2' (C_{20} - C_2) = D_2 \frac{\partial C_2}{\partial x} \tag{21}$$

$$\ell_1' \, C_1 = -D_1 \frac{\partial C_1}{\partial x} \tag{22}$$

where the bulk values of C_2 and C_1 at the chloride side and the water side, respectively, are zero, ℓ_1 and ℓ_2 are the mass transfer coefficients from the chloride side (tube interior), and ℓ_1' and ℓ_2' are the same coefficients at the water side (annulus).

The effective diffusion coefficients in Eqs. 13 and 14 (and in Eqs. 19 through 22) are functions of the local porous structure. For simplicity, we have adopted the random capillary model (Gavalas, 1980) with capillaries of uniform initial radius a_o. Then, the local capillary radius is related to the local void fraction by the relation:

$$\epsilon(x, t) = 1 - \exp(-2\pi\lambda a^2) \tag{23}$$

The two effective diffusion coefficients are then expressed in terms of ϵ by the simple, often-used relation:

$$D_i = \frac{\epsilon}{\tau} A \left(\frac{T}{M_i}\right)^{1/2} a \qquad i = 1,2 \tag{24}$$

where A is the constant in the Knudsen diffusion coefficient, M_1 and M_2 are the molecular weights of chloride and water, and τ is the empirical tortuosity.

Numerical Results and Discussion

Simulations were performed for SiO_2 formation at 800°C. Among the various rate constants, only k_1 could be estimated from previous reports. Hair and Hertl (1969) reported values of k_1 in the range 300-500°C. Recent thermogravimetric experiments in our laboratory provided additional values up to 600°C. Extrapolating these measurements to 800°C, we estimated the base value of k_1 in Table 1. The thermogravimetric experiments also indicated that k_2 is lower than k_1 by a factor of 3 to 10. In our calculations, we varied k_2/k_1 between 0.1 and 1. The constants k_3 and k_4, for which no information was available, were varied together between 0 and 10. The initial surface concentration of silanol groups (—OH) was estimated from the aforementioned thermogravimetric experiments to be between 3 and 5/nm^2 for Vycor annealed at 600°C, while for Vycor annealed at 800°C the literature suggests a lower value, 1—2/nm^2 (Hair and Hertl, 1969, 1973; Peri and Hensley, 1968). In our experiments, the Vycor tubes were pretreated at 600°C for several hours and then heated to 800°C just before the beginning of deposition. Because the exposure to 800°C before deposition was minimal, we esimated the concentration of the —OH groups to be in the range 1.5—4.5/nm^2 and made parametric calculations with several values in this range. The Nusselt number was estimated around 4 for both the internal and external flows (Welty et al., 1984), while the bulk diffusion coefficients were estimated using the equation given by Bird et al. (1960, p. 505). Table 1 lists all other parameter values used in the calculations. Numerical solutions of Eqs. 13 through 22 were obtained to explore the effect of various parameters and compare with the microprobe traces. The time evolution equations (Eqs. 15 through 17) were integrated by a fourth-order Runge-Kutta routine. Each evaluation of the right side of these equations required the solution of the linear boundary value problem (Eqs. 13-14 and 19-22). This solution was carried out by difference spatial discretization and solution of the resulting linear system by Gaussian elimination. Each run was terminated when the local radius decreased to one-fifth of its original value (4Å).

Table 1. Model Parameter Values

k_1	$2.45\times10^{11}\exp(-22{,}000/RT)$ cm^3/min-mol
k_4	5 cm^3 solid deposit/min-mol
k_2	$0.1k_1$
k_3	k_4
C_1^0	0.25 atm/RT
C_2^0	0.1 atm/Rt
τ	3
ϵ_o	0.3
a_o	20×10^{-8} cm
L	0.11 cm
S_o	3×10^6 cm^2/cm^3
v	29 cm^3/mol
ρ_p	1.47 g/cm^3
S^0_{OH}	(OH sites/nm^2) $\frac{1}{6.023\times10^9} S_o$ in mol/cm^3
OH/nm^2	2
ℓ_i	$\frac{Nu\,D_i,\ \text{bulk}}{d}$, cm/min
ℓ_i'	$\frac{Nu'\,D_i,\ \text{bulk}}{d}$, cm/min
$Nu \cong Nu'$	4
$d-d'_{\text{equivalent}}$	0.5 cm
D_{H_2O}, bulk	5.2 cm^2/s at 800°C (estimated using Eq. 16.3-1 from Bird et al., 1960, p. 505)
D_{SiCl_4}, bulk	2 cm^2/s at 800°C (estimated using Eq. 16.3-1 from Bird et al., 1960, p. 505)

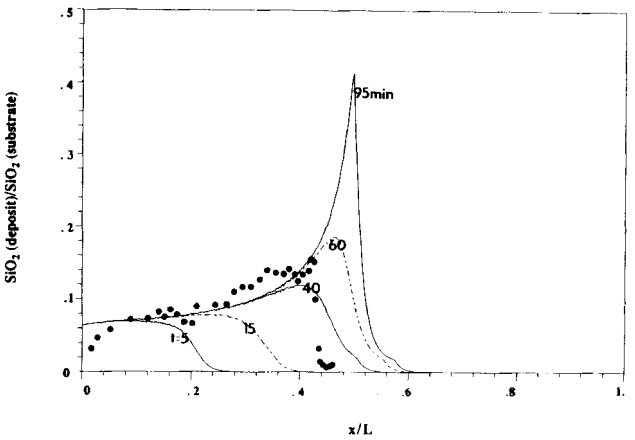

Figure 7. Simulated evolution of SiO_2 deposit at 800°C in opposing reactants geometry.

Using the parameter values in Table 1 except $C_{10} = 0.3$ atm/RT, $C_{20} = 0.07$ atm/RT (as in the experiments of Figure 5). (●) Data of Figure 5 replotted for comparison.

At $t = 0$, the rate of condensation reactions is zero because there are no chloride groups and because the —OH groups after lengthy heat pretreatment are too far from each other or prevented to react because of steric hinderances (this subtlety is not described by Eq. 9). Thus, at $t = 0$, the last terms in Eqs. 14, 15 and 16 are indeterminate. To initialize the integration we have set these two terms equal to zero until $\epsilon_o - \epsilon$ becomes 0.01.

Figure 7 shows the density profile of the deposit layer at different times during deposition. The profile initially decreases monotonically with distance from the chloride side, but later develops a maximum that gradually steepens as pore plugging is approached. As mentioned earlier in the discussion of Figure 5, the value of 0.17 for SiO_2(deposit)/SiO_2(substrate) at the position of pore plugging measured in the electron probe scans contains several errors, the most important of which is the limited resolution of the electron microprobe. Thus, the true value of this ratio is expected to be higher than 0.17 but lower than the value 0.43 calculated for complete pore filling, assuming a deposit density of 2.1 g/cm^3. Taking a value ~0.2 as an estimate, we may consider pore plugging to occur at $t \approx 60$ min when the peak of the profile reaches that value. For comparison, the experimental points of Figure 5 have been included in Figure 7.

Figures 8-11 show the effect of the parameters k_2/k_1, k_3, S^o_{OH}, and C_{10}. Figure 8 shows the normalized density profile

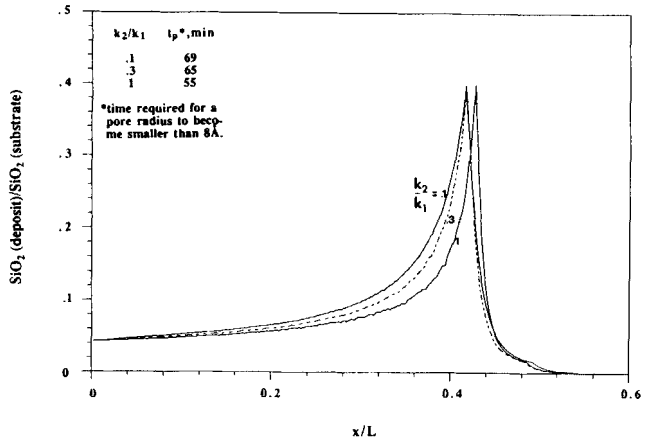

Figure 8. Simulated density profiles of the SiO_2 layers at the end of deposition for three different values of k_2/k_1.

Parameters values are in Table 1.

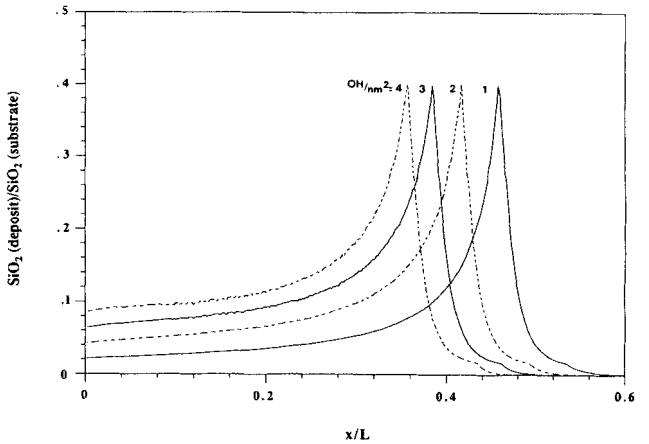

Figure 10. Simulated density profiles for different values of initial OH concentrations.

of the deposit layer vs. dimensionless distance from the chloride side for different values of the ratio k_2/k_1. Keeping k_1 constant, the film thickness and the time required for pore plugging increase with decreasing values of k_2/k_1. Clearly, with lower hydrolysis rates, the regeneration of the —OH groups necessary for continuation of the reaction becomes slower, slowing down the overall process. Figure 9 shows the effect of the condensation reactions (Eqs. 4 and 5). As k_3 and k_4 increase, the film moves away from the chloride side and the time for complete pore filling increases from 65 min for $k_3=0$ to 74 min for $k_3=20$ cm^3/min·mol. As expected, more rapid condensation reactions bring down the concentration of reactive sites and slow down the overall process. Moreover, the condensation reactions have a larger stoichiometric coefficient for —OH groups, and therefore tend to decrease the [—OH]:[—Cl] ratio moving the reaction region toward the water side. By contrast, an increase of S^o_{OH} causes the deposit layer to move toward the chloride side and the tail thickness to increase (Figure 10). As OH concentration increases, more chloride can react with the Vycor surface in the absence of H_2O vapor causing the increase of the tail thickness. Moreover, due to the increased chloride consumption, the reaction front is moved toward the chloride side causing the shift of the deposit position. Finally, increasing the concentration of one of the reactants (such as chloride) causes the deposit layer to move in the direction of the other reactant and shortens the time required for pore plugging (Figure 11). Additional calculations not included in the figures show that the width of the deposit layer decreases while the time for pore filling increases with decreasing initial pore size. For example, the times to complete pore filling were 69 and 95 min for initial pore diameters of 40 Å and 25 Å, respectively.

Despite the success of the transient model in describing the growth of the deposit, it is interesting to examine the ability of conventional pseudosteady kinetics to describe deposition. For this purpose, we have formulated a deposition model based on pseudosteady kinetics (Appendix) and carried out a number of calculations to obtain deposit layer profiles up to the time of pore plugging. In this model the rate was taken as:

$$r = kC_1^{\alpha}C_2^{\beta}$$

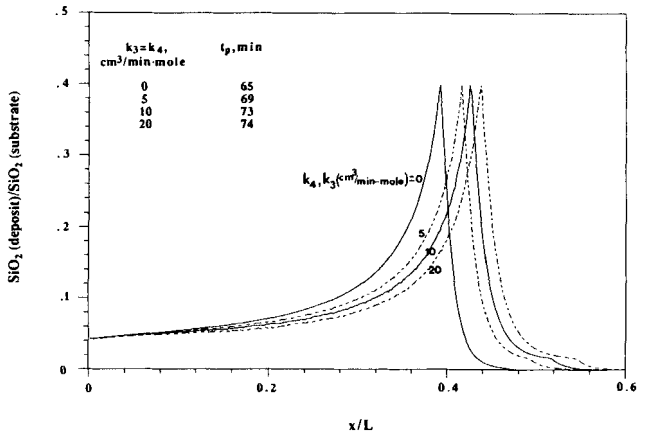

Figure 9. Effect of condensation reactions (Eqs. 4 and 5) on deposit profiles at the end of deposition.

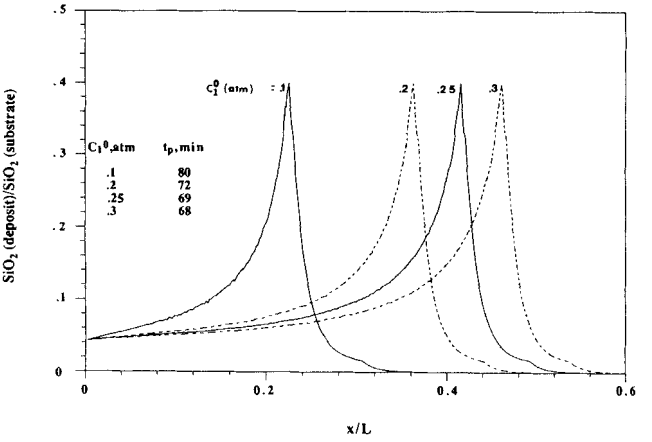

Figure 11. Effect of chloride concentration on deposit profile.

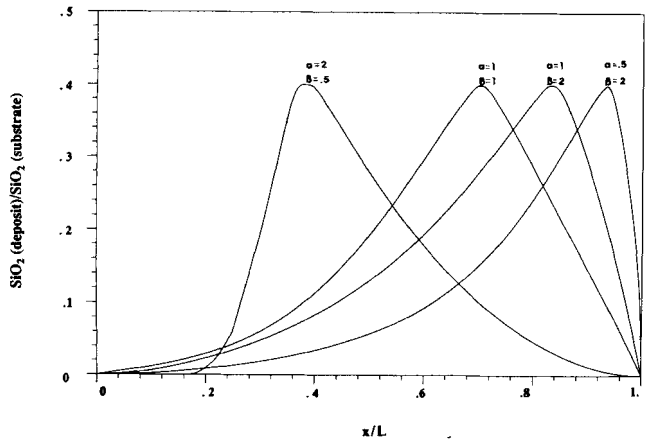

Figure 12. Simulated density profiles of SiO_2 layers at the end of deposition for four different combinations of reaction orders α and β using the rate expression $r = kC_{10}^{\alpha} C_{20}^{\beta}$.

Deposition conditions are those for the experiment in Figure 5.

Numerous runs were performed combining various values of α and β with a value of k such that pore closure takes place at approximately 60 ~ 90 min. None of these simulations was able to reproduce the experimental deposit characteristics. Figure 12 is an example from these simulations for the conditions of the experiment in Figure 5. This figure shows the deposit profiles for various values of α and β and a common value of k chosen to match the experimental time for pore closure. The profiles calculated from the model fail to match the finite deposit density at $x = 0$. The position of the peak could be made to match the experimental position by increasing α/β, but then the profile does not have the steep decline after the peak. On the other hand, by decreasing α/β, it is possible to match the steep drop of the profile but then the peak location moves too far to the right.

A final word of caution is in order about the scope of the deposition model. The model developed here is confined to the description of the growth of the deposit layer and can predict the gross features of the final deposit density profile. This information is of some value in understanding qualitatively the effect of parameters such as pore size and concentration of reactants on the membrane permeance. However, the quantitative prediction of membrane permeance requires measurement of the permeability of various gases as a function of deposit density over the whole range of densities encountered across the membrane layer. This experimental program has not been carried out.

Conclusions

Silica and alumina layers prepared in the opposing reactants geometry by the hydrolysis of the chlorides possess highly asymmetric shape. The deposit density increases gradually from the chloride side, passes through a maximum, and steeply decreases to zero well before the water side. Pore plugging is attained at a nonzero void fraction, evidently due to a percolative interruption of connectivity. A deposition mechanism suggested by previous studies has been adopted involving reaction of the gaseous chloride with silanol groups on the surface, reaction of water vapor with chloride groups of the surface, and condensation of two silanol groups or a silanol and a chloride group to form siloxane bonds. The transient kinetics associated with these reactions were introduced into a model employing a classical description of diffusion and pore closure. The numerical results obtained with this model describe well the location and shape of the deposit layer, but are not capable of describing the interruption of connectivity at a nonzero void fraction. The calculations show that the geometry of the deposit layer is relatively insensitive to the kinetic parameters, but it is more sensitive to the pore size and the density of silanol groups of the Vycor substrate. A pseudosteady kinetic model failed to predict the qualitative trends observed in the experiments.

Acknowledgment

Dr. S. W. Nam contributed in the development of the homogeneous model. Support was provided by the Department of Energy with UCR Grant DE-FG22-89PC89765 and Contract DE-AC21-90MC26365.

Notation

a = pore radius, cm
a_o = initial pore radius, cm
C_1 = gas-phase chloride concentration, mol/cm^3 pore volume
C_2 = gas-phase water concentration, mol/cm^3 pore volume
C_i^0 = chloride or water concentration at the bubbler, mol/cm^3
d = outside diameter of Vycor tube, cm
$d'_{\text{equivalent}}$ = equivalent hydraulic diameter of outside flow, cm
D_i = Knudsen diffusivity of species i, cm^2/min
$D_{i,\text{bulk}}$ = binary diffusivity of species i, cm^2/min
k = reaction rate constant used in the pseudosteady state kinetics
k_1, k_2 = reaction rate constants, cm^3 pore volume/min·mol
k_3, k_4 = reaction rate constants, cm^3 deposit/min·mol
L = thickness of substrate Vycor tube, cm
M_i = molecular weight of species i
Nu = Nusselt number
q = thickness of deposit layer perpendicular to pore wall, cm
R = gas constant
r = reaction rate used in the pseudosteady state kinetics, mol/cm^2·min
r_i = rate of ith reaction ($i = 1, \ldots, 4$); mol/cm^3·min
S_{OH} = —OH concentration, mol/cm^3
S_{Cl} = —Cl concentration, mol/cm^3
S_{OH}^0, S_{Cl}^0 = initial concentrations of OH and Cl, mol/cm^3
S = surface area per unit volume, cm^2/cm^3
T = temperature, K
v = molar volume of deposit, cm^3/mol
x = distance measured from inside wall of substrate tube, cm

Greek Letters

α = reaction order of chloride (when using the expression $r = kC_1^{\alpha}C_2^{\beta}$)
β = reaction order of water (when using the expression $r = kC_1^{\alpha}C_2^{\beta}$)
ϵ = void fraction of substrate
ϵ_o = initial void fraction of substrate
λ = parameter of the random capillary model, cm^{-2}
τ = tortuosity
ϕ = deposit volume fraction

Literature Cited

Armistead, C. G., and J. A. Hockey, "Reactions of Chloromethyl-

silanes with Hydrated Aerosil Silicas," *Trans. Farad. Soc.*, **63**, 2549 (1967).
Bird, R. B., W. E. Stewart, and E. N. Lightfoot, *Transport Phenomena*, Wiley, New York (1960).
Bunker, B. C., D. M. Haaland, T. A. Michalske, and W. L. Smith, "Kinetics of Dissociative Chemisorption on Strained Edge-Shared Surface Defects on Dehydroxylated Silica," *Surf. Sci.*, **222**, 95 (1989).
Carolan, M., and J. N. Michaels, "Chemical Vapor Deposition of Yttria Stabilized Zirconia on Porous Substrates," *Solid State Ionics*, **25**, 207 (1987).
Gavalas, G. R., "A Random Capillary Model With Application to Char Gasification at Chemically Controlled Rates," *AIChE J.*, **26**, 577 (1980).
Gavalas, G. R., C. E. Megiris, and S. W. Nam, "Deposition of H_2-permselective SiO_2 Films," *Chem. Eng. Sci.*, **44**, 1829 (1989).
Hair, M. L., and W. Hertl, "Reactions of Chlorosilanes with Silica Surfaces," *J. Phys. Chem.*, **73**, 2372 (1969).
Hair, M. L., and W. Hertl, "Chlorination of Silica Surfaces," *J. Phys. Chem.*, **77**, 2070 (1973).
Iller, R. K., *The Chemistry of Silica*, Wiley, New York (1979).
Isenberg, A. O., "Energy Conversion via Solid Electrolyte Electrochemical Cells at High Temperatures," *Solid State Ionics*, **314**, 431 (1981).
Morrow, B. A., and I. A. Cody, "Infrared Studies of Reactions on Oxide Surfaces: 5. Lewis Acid Sites on Dehydroxylated Silica," *J. Phys. Chem.*, **80**, 1995 (1976).
Peglar, R. J., F. H. Hambletton, and J. A. Hockey, "Structure Surface and Catalytic Properties of the SiO_2/BCl_3, $SiO_2/AlMe_3$ and $SiO_2/AlCl_3$ Systems," *J. Catal.*, **20**, 309 (1971).
Peri, J. B., "Infrared Study of Adsorption of Carbon Dioxide, Hydrogen Chloride and Other Molecules on "Acid" Sites on Dry Silica-Alumina and γ-Alumina," *J. Phys. Chem.*, **70**, 3168 (1966).
Peri, J. B., and A. L. Hensley, Jr., "The Surface Structure of Silica Gel," *J. Phys. Chem.*, **72**, 2926 (1968).
Sahimi, M., G. R. Gavalas, and T. T. Tsotsis, "Statistical and Continuum Models of Fluid-Solid Reactions in Porous Media," *Chem. Eng. Sci*, **45**, 1443 (1990).
Sotirchos, S. V., "Dynamic Modelling of Chemical Vapor Infiltration," *AIChE J.*, **37**, 1365 (1991).
Tsapatsis, M., S. J. Kim, S. W. Nam, and G. R. Gavalas, "Synthesis of Hydrogen Permselective SiO_2, TiO_2, Al_2O_3 and B_2O_3 Membranes from the Chloride Precursors," *I&EC Res.*, **30**, 2152 (1991).
Welty, J. R., C. E. Wicks, and R. E. Wilson, *Fundamentals of Momentum, Heat and Mass Transfer*, Wiley, New York (1984).
Wong, P., and M. Robinson, "Chemical Vapor Deposition of Polycrystalline Al_2O_3," *J. Amer. Ceram. Soc.*, **53**, 617 (1970).

Appendix: Model Based on the Pseudosteady-State Approximation for Surface Species

Consider the chemical vapor deposition reaction:

$$\nu_1 A_1(g) + \nu_2 A_2(g) - \text{Solid} \tag{A1}$$

occurring within the walls of porous glass in an opposing reactants geometry.

Diffusion and reaction in a porous glass can be described by the equations:

$$\frac{\partial}{\partial x}\left[(D_1(\epsilon)\frac{\partial c_1}{\partial x}\right] = \nu_1 S(\epsilon) r \tag{A2}$$

$$\frac{\partial}{\partial x}\left[(D_2(\epsilon)\frac{\partial c_2}{\partial x}\right] = \nu_2 S(\epsilon) r \tag{A3}$$

with boundary conditions:

$$\text{at } x=0 \qquad \ell_1(C_{10}-C_1) = -D_1\frac{\partial C_1}{\partial x},\ \ell_2 C_2 = D_2\frac{\partial C_2}{\partial x} \tag{A4}$$

$$\text{at } x=L \qquad \ell_2'(C_{20}-C_2) = D_2\frac{\partial C_2}{\partial x},\ \ell_1' C_1 = -D_1\frac{\partial C_1}{\partial x} \tag{A5}$$

where we used the pseudosteady-state approximation to delete the accumulation terms. The rate of increase of the deposit solid layer is:

$$\frac{\partial q}{\partial t} = vr \tag{A6}$$

with initial condition:

$$\text{at } t=0 \quad q=0 \tag{A7}$$

We use the following rate expression:

$$r = kC_1^{\alpha}C_2^{\beta} \tag{A8}$$

The random pore model with single initial radius a_o is used and additionally here we make use of the relation:

$$S(q) = -\frac{d\epsilon(q)}{dq} = 4\pi(1-\epsilon)[\lambda(a_o - q)] \tag{A9}$$

since in that model one needs the surface area.

The above equations are solved numerically using central finite difference. The equations are discretized to give a set of nonlinear algebraic equations, which are solved by iteration based on the Newton-Raphson method.

Manuscript received Nov. 27, 1991, and revision received Mar. 19, 1992.